

# Comparison between spatial and temporal wall oscillations in turbulent boundary layer flows

Martin Skote†

School of Mechanical & Aerospace Engineering, Nanyang Technological University, 50 Nanyang Avenue, Singapore 639798, Singapore

(Received 27 December 2012; revised 25 June 2013; accepted 1 July 2013)

Direct numerical simulations have been performed to study the drag reduction resulting from spatial oscillations of a segment of the wall under a turbulent boundary layer. The oscillating motion is imposed by utilizing a streamwise modulated spanwise wall forcing. The results are compared with earlier simulations using temporal oscillations with an identical segment and forcing amplitudes, and with a frequency related to the wavelength through a convective velocity. Two different oscillation amplitudes with equal oscillation wavelength have been used, which allows for a direct comparison between a relatively weak and strong forcing of the flow. The weaker forcing results in 25 % drag reduction while the stronger forcing, with twice the amplitude, yields 41 % drag reduction. Comparison with the temporal cases reveals drastically improved energy savings for the spatial oscillation technique, in accordance with earlier channel flow investigations. The streamwise variation of spanwise shear is shown to follow the analytical solution to the laminar Navier–Stokes equations derived under the assumption of constant friction velocity. Furthermore, the spanwise velocity profiles at various phases are compared with the analytical solution, and show very good agreement. The downstream development of the spatial Stokes layer thickness is theoretically estimated to be  $\sim x^{1/15}$ , in general agreement with the simulation data. The spatial variation of the spanwise Reynolds stress is investigated and compared with the variation in time for the temporal wall forcing cases. The controversy regarding a zero or non-zero production of spanwise Reynolds stress in the temporal case is elucidated. In addition, comparison with the spatial case reveals that a second production term originating from the downstream variation of the spanwise wall velocity has a negative contribution to the production, and hence relates to the larger drag reduction in the case of spatial forcing.

**Key words:** Flow control, turbulent boundary layers, drag reduction

---

## 1. Introduction

Reducing drag forces would have an immense impact on the economy of many engineering applications. However, although many control strategies have been investigated in the past, both feedback-control techniques (Kasagi, Suzuki & Fukagata 2009) and open-loop techniques in the form of wall motion or body force (Karniadakis & Choi 2003), no practical implementation has yet been realized successfully. One of

† Email address for correspondence: [mskote@ntu.edu.sg](mailto:mskote@ntu.edu.sg)

the simplest methodologies involves spanwise oscillation (either temporal, spatial, or in the form of travelling waves), which in reality is difficult to apply to an aircraft wing, for example. Thus, before technologies can emerge for large-scale implementation on real-life machinery, a better understanding of the underlying mechanisms behind the drag reduction (DR) is desirable. The purpose of this paper is to advance this understanding by comparing two different types of oscillation: temporal and spatial.

The temporal form of oscillation, which is the most straightforward to implement, and therefore was the first technique to be utilized by researchers, can be applied via a wall velocity ( $W$ ) in the spanwise direction in the form of

$$W = W_m \sin(\omega t), \quad (1.1)$$

where  $W_m$  is the maximum wall velocity and  $\omega$  is the angular frequency of the wall oscillation, which is related to the period ( $T$ ) via  $\omega = 2\pi/T$ .

The first studies of turbulent flows over an oscillating wall were performed numerically using direct numerical simulation (DNS) of channel flow by Jung, Mangiavacchi & Akhavan (1992). During the following 20 years a number of DNSs of the channel flow with temporal spanwise oscillations have been conducted (Baron & Quadrio 1996; Choi, Xu & Sung 2002; Quadrio & Ricco 2003, 2004; Xu & Huang 2005; Ricco & Quadrio 2008; Ricco *et al.* 2012; Toubert & Leschziner 2012).

The first experimental evidence that confirmed Jung's DNS results was provided by Laadhari, Skandaji & Morel (1994) and Skandaji (1997), who applied the oscillation technique to the boundary layer flow. Since then, most of the experimental investigations have been focused on the boundary layer (Trujillo, Bogard & Ball 1997; Choi & Clayton 2001; Choi 2002; Di Cicca *et al.* 2002; Ricco 2004; Ricco & Wu 2004).

Pipe flow also exhibits DR when the wall undergoes oscillations. Choi & Graham (1998) were the first to experimentally investigate the oscillating pipe flow. Subsequently, both DNS (Nikitin 2000; Quadrio & Sibilla 2000; Duggleby, Ball & Paul 2007) and experiments (Auteri *et al.* 2010) have been conducted.

Yudhistira & Skote (2011) performed the first DNS of turbulent boundary layers over an oscillating wall, and the DR development downstream followed that observed from experiments by Ricco & Wu (2004). The sensitivity of the Reynolds shear stress profiles to the turbulence statistics sampling time was investigated, and some inconsistency in earlier experimental findings could be explained. Skote (2012) chose lower oscillating amplitudes to demonstrate that a positive energy budget was possible, and extensive comparisons with experimental data were performed. The simulations investigated in the present work are conducted using the same numerical code, but with a spatial wall forcing instead of a temporal one, as explained below.

Recently, some researchers have considered a steady variation in the streamwise direction along the plate in the form of

$$W = W_m \sin(\kappa x), \quad (1.2)$$

where  $\kappa$  is the wavenumber of the spatial oscillation, which is related to the wavelength ( $\lambda_x$ ) via  $\kappa = 2\pi/\lambda_x$ .

The investigations of spatial oscillation have so far only been performed using DNS of channel flow by Viotti, Quadrio & Luchini (2009) and of boundary layer flow by Skote (2011). An improved energy saving compared to temporal oscillations was obtained in both of these studies.

The combination of spatial and temporal wall oscillation (streamwise travelling waves) in a channel flow was studied (via DNS) by Quadrio, Ricco & Viotti (2009).

However, only marginal improvement on the DR (compared to the stationary forcing) was obtained. The theoretical and numerical studies were recently further developed by Quadrio & Ricco (2011). The only experimental data so far for this type of wall forcing are provided by Auteri *et al.* (2010), who applied the streamwise travelling wave on the pipe flow.

In the present paper results are presented from DNS of boundary layer flow with a steady spanwise wall velocity which is varying in the streamwise direction according to (1.2), and are compared to the results (Skote 2012) from a temporally oscillating spanwise wall velocity according to (1.1). Oscillation parameters have been chosen in order to facilitate a direct comparison. Thus the values of  $W_m$  are kept identical to the previous temporal oscillation cases, and the chosen wavenumber  $\kappa$  corresponds to the angular frequency since they are related through a convection velocity  $\mathcal{U}_w$  according to  $\kappa \mathcal{U}_w = \omega$ .

Hence, in the present investigation, four simulations are compared: two cases with the forcing according to (1.1) and two cases according to (1.2). For each forcing type, two different wall velocities have been used. The results from the temporal forcing were presented in Skote (2012) with extensive comparison to experimental results. Thus, in the present paper we focus on the comparison between the two new simulations using spatial forcing with the previously investigated temporal oscillating cases.

Specific flow features of the spatial forcing case we consider in the present work, which have not been investigated before, either by Viotti *et al.* (2009) for channel flow or by Skote (2011) for boundary layer flow, are:

- (i) spatial development of spanwise shear;
- (ii) streamwise transients of spanwise velocity profiles;
- (iii) downstream development of the spatial Stokes layer thickness;
- (iv) comparison of Reynolds stresses for spatial and temporal forcing;
- (v) phase-averaged spanwise Reynolds stress, and its transients;
- (vi) production of the spanwise Reynolds stress, and its relation to DR.

The paper is organized as follows. In §2 the numerical method and simulation related issues are discussed. The analytical results considering the spanwise flow, which is approximated with the laminar equations, are presented in §3. The DR and power budget are discussed in §4, while turbulence statistics are presented in §5. Lastly, conclusions are drawn in §6.

## 2. Numerical method and simulation parameters

The numerical code and grid are the same as in the previous simulations of a spatially oscillating turbulent boundary layer reported by Skote (2011). Two new simulations of turbulent boundary layers subjected to a steady spanwise wall velocity, which is varying in the streamwise direction according to (1.2), have been performed with different wall velocities. A third simulation uses the higher of the two wall velocities, but with a larger grid resolution, to prove that the resolution is sufficient. The code was developed at KTH, Stockholm (Chevalier *et al.* 2007). A simulation of a turbulent boundary layer at  $Re_\theta = 2500$  was performed by Schlatter *et al.* (2009), with results in excellent agreement with experimental data at the same Reynolds number. An outline of the numerical scheme is presented in §2.1, the various parameters used and the resolution are presented next in §2.2, where the implementation of the wall motion is also presented.

### 2.1. Numerical scheme

A pseudospectral method is employed, with Fourier discretization used in the streamwise and spanwise directions and Chebyshev polynomials in the wall-normal direction. The simulations start with a laminar boundary layer at the inflow which is triggered to transition by a random volume force near the wall (referred to as the trip in the following). Details can be found in Yudhistira & Skote (2011).

A fringe region is added at the end of the computational domain to enable simulations of spatially developing flows (see figure 1). In this region the flow is forced from the outflow of the physical domain to the inflow. In this way the physical domain and the fringe region together satisfy periodic boundary conditions. The implementation is done by adding a volume force

$$F_i = \lambda(x)(\hat{u}_i - \tilde{u}_i) \quad (2.1)$$

to the Navier–Stokes equations,

$$\frac{\partial \tilde{u}_i}{\partial t} + \tilde{u}_j \frac{\partial \tilde{u}_i}{\partial x_j} = -\frac{1}{\rho} \frac{\partial \tilde{p}}{\partial x_i} + \nu \frac{\partial^2 \tilde{u}_i}{\partial x_j^2} + F_i. \quad (2.2)$$

The force  $F_i$  acts only in the fringe region,  $\hat{u}_i$  is the laminar inflow velocity profile the solution  $\tilde{u}_i$  is forced to, and  $\lambda(x)$  is the strength of the forcing. The form of the fringe function is designed to have minimal upstream influence and is given by

$$\lambda(x) = \lambda_{\max} f(x) \quad (2.3)$$

with

$$f(x) = S\left(\frac{x - x_{\text{start}}}{\Delta x_{\text{rise}}}\right) - S\left(\frac{x - x_{\text{end}}}{\Delta x_{\text{fall}}} + 1\right). \quad (2.4)$$

Here  $\lambda_{\max}$  is the maximum strength of the fringe,  $x_{\text{start}}$  and  $x_{\text{end}}$  denote the spatial extent of the region where the fringe is non-zero, and  $\Delta x_{\text{rise}}$  and  $\Delta x_{\text{fall}}$  are the rise and fall distance of the fringe function respectively.  $S(x)$  is a continuous step function that rises from zero for negative  $x$  to unity for  $x \geq 1$ . The expression for  $S(x)$ , which has the advantage of having continuous derivatives of all orders, is

$$S(x) = \begin{cases} 0, & x \leq 0, \\ 1/(1 + e^{(1/(x-1)+1/x)}), & 0 < x < 1, \\ 1, & x \geq 1. \end{cases} \quad (2.5)$$

The function  $f(x)$  is also utilized in the implementation of the wall oscillation described in § 2.2 below.

The time integration is performed using a third-order Runge–Kutta scheme for the nonlinear terms and a second-order Crank–Nicolson method for the linear terms. A 3/2 rule is used to remove aliasing errors from the evaluation of the nonlinear terms when calculating FFTs in the wall-parallel plane.

### 2.2. Numerical parameters

All quantities are non-dimensionalized by the free stream velocity ( $U$ ) and the displacement thickness ( $\delta^*$ ) at the starting position of the simulation ( $x = 0$ ), where the flow is laminar. The Reynolds number is set by specifying  $Re_{\delta^*} = U\delta^*/\nu$  at  $x = 0$ . In all the simulations presented here,  $Re_{\delta^*} = 450$ . The computational box is 600 in simulation length units ( $\delta^*$ ) long (including 100 units for the fringe), 30 units high and 34 units wide.

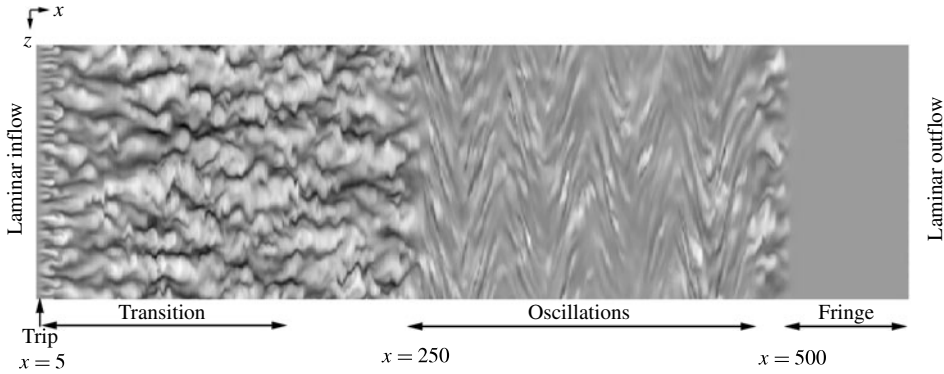


FIGURE 1. Horizontal plane ( $y = 0.5$ ) in the computational box. The dark grey indicates low-speed regions and lighter shades indicate high-speed patches. The laminar outflow is equal to the inflow, so periodic boundary conditions are used in the horizontal plane. The size of the computational box horizontally is 600 in  $x$  and 34 in  $z$  (in units of  $\delta^*$ ). The figure is compressed by a factor of five in the downstream ( $x$ ) direction.

As the fringe starts at  $x = 500$ , only results up to  $x = 470$  will be utilized to avoid any upstream influence of the fringe. The transition region is roughly between  $x = 5$  (where the trip is located, see figure 1) and  $x = 150$ . Thus, the region of a fully developed turbulent boundary layer, free from any influence of the numerical method, is  $x = 150\text{--}470$ . The Reynolds number based on the momentum thickness ( $Re_\theta$ ) varies between 418 and 750 in this region for the unmanipulated (reference) boundary layer. In inner scaling (based on the friction velocity at  $x = 250$ ), the region amounts to  $\sim 7000$  wall units.

The spatial wall oscillation in the present simulations is applied in the spanwise direction at a particular region in the streamwise direction. Therefore, the form of this boundary condition is given by

$$w|_{y=0} = W_m f(x) \sin[\kappa(x - x_{start})], \quad (2.6)$$

where a profile function  $f(x)$  is utilized to select the domain where the oscillation takes place, and is the same profile function as used for the fringe region (see (2.4)), with  $x_{start}$ ,  $x_{end}$ ,  $x_{rise}$  and  $x_{fall}$  set to 250.3, 483.0, 10.0 and 10.0 respectively.

A horizontal plane of the full computational box (stretched in the spanwise direction) is shown in figure 1, where low-speed streaks near the wall are visualized. The spatial oscillations are clearly revealed and are a direct result of the streamwise modulated spanwise wall forcing. The figure illustrates how the periodic boundary conditions can be utilized due to the numerical fringe region at the end of the computational box, where the laminar flow is restored using the forcing provided by (2.1).

In the simulation presented here the wavenumber ( $\kappa$ ) is set to 0.108, which in wall units corresponds to a wavelength of  $\lambda_x^+ = 1320$ , while two different values for the maximum wall velocity ( $W_m$ ) were used, 0.3025 and 0.605 respectively, which in wall units corresponds to  $W_m^+ = 6$  and  $W_m^+ = 12$ , based on  $u_\tau^0$  where the wall forcing starts ( $x = 250$ ). In the following the lower amplitude case will be referred to as case 1, while the higher amplitude case is denoted case 2. As described above, the wall forcing is applied between  $x = 250.3$  and  $x = 483.0$  in simulation coordinates,

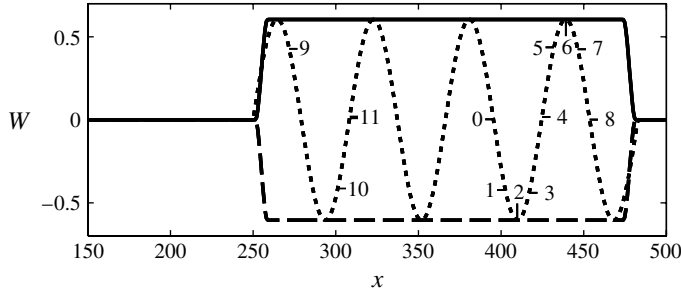


FIGURE 2. Downstream variation of the wall velocity: —, at maximum positive wall velocity; — —, at maximum negative wall velocity;  $\cdots$ , constant (in time) wall velocity varying downstream. The positions marked 0–11 will be used to compare various quantities at different phases of the spatial wall oscillation in §§ 3 and 5.

which corresponds to four periods, or a total length of applied wall motion of 5000 in wall units.

The results will be compared with temporal oscillation simulations taken from Skote (2012). In that case the wall oscillation is described by (1.1) and the form of this boundary condition is given by

$$w|_{y=0} = W_m f(x) \sin[\omega(t - t_{start})]. \quad (2.7)$$

The parameter  $\omega$  is the angular frequency of the wall oscillation, which is related to the period by  $\omega = 2\pi/T$ . The angular frequency ( $\omega$ ) of the wall oscillation is set to 0.0545, which in wall units corresponds to  $T^+ = 132$ . The amplitudes were set identically to cases 1 and 2 as described above. In the following the lower amplitude case will be referred to as temp 1 while the higher amplitude case is called temp 2. (These are the simulations referred to as cases 1 and 2 in Skote 2012.)

The wavelength ( $\lambda_x$ ) in the simulations presented here was chosen so that  $\lambda_x^+ = \mathcal{W}_w^+ T^+$ . An estimated value of  $\mathcal{W}_w^+ = 10$  was shown to relate the temporal and spatial transients in a temporally oscillating boundary layer by Skote (2012).

The streamwise modulation of the wall velocity is illustrated in figure 2 (dotted line) together with the corresponding temporally oscillating wall velocity at the instant of maximum positive and maximum negative wall velocity. The numbered positions in the figure will be utilized later in the text.

Two different resolutions were used for the simulations to ensure that the results would be completely grid-independent. The cases from Skote (2012) (temp 1 and temp 2) were simulated with a resolution of 800 modes in the streamwise direction, 201 modes in the wall-normal direction, and 144 modes in the spanwise direction.

The present DNS data (cases 1 and 2) were simulated using the same grid as above, and case 2 was then simulated using a grid of size  $1000 \times 217 \times 192$ , yielding a resolution in wall units of  $\Delta X^+ \times \Delta Z^+ \times \Delta Y_{min}^+ = 13.6 \times 4.0 \times 0.036$ . Note that unless otherwise stated, the + superscript indicates that the quantity is made non-dimensional with the friction velocity of the unmanipulated boundary layer (the reference case), denoted  $u_\tau^0$ , and the kinematic viscosity ( $\nu$ ).

The velocity profile at the position  $x = 400$ , i.e. in the region of maximum DR, is shown in figure 3(a) for the two grids. The difference is very small and is due to the small variation (0.8%) in friction velocity between the two resolutions. Indeed, if the same  $u_\tau$  is used as the scaling velocity, the velocity profiles completely overlap.

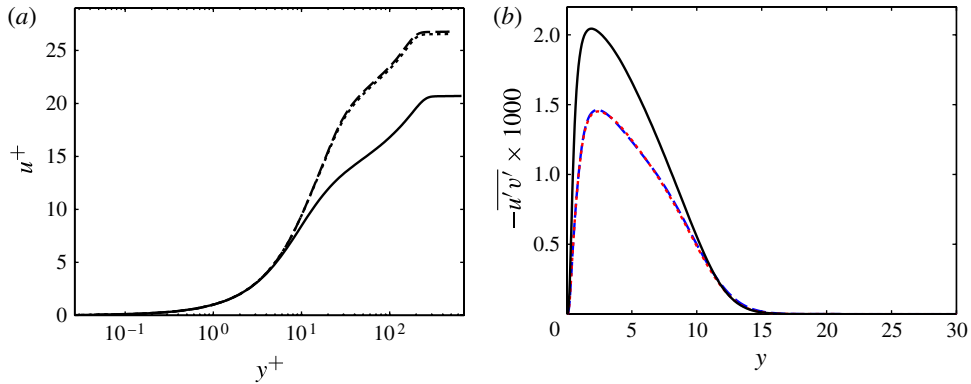


FIGURE 3. (Colour online) (a) Velocity profiles (case 2) at the position  $x = 400$  for the two resolutions. (b) Reynolds shear stress profiles (case 1) at  $x = 400$ . Lines: —, reference case; - - (blue), statistics for  $t = 5000$ – $13\,000$ ; ··· (red), statistics for  $t = 13\,000$ – $22\,000$ .

The sampling time for the reference case was 12 000 in time units ( $\delta^*/U$ ), corresponding to 13 700 in viscous units, started only after a stationary flow (in the statistical sense) was reached. In the cases with wall forcing, the total sampling time was 17 000 (19 400 in viscous units) after an initial simulation time of 5000 with oscillations.

In the previous simulation by Yudhistira & Skote (2011) it was shown that the most sensitive statistical quantity with respect to the length of sampling time is the Reynolds shear stress. Thus, as a measure of the grade of convergence of the turbulence statistics the Reynolds shear stresses from two different time intervals are shown in figure 3(b). In this case, we chose the unscaled quantity and linear scaling of the wall-normal coordinate ( $y$ ) to demonstrate the sufficiently high computational box. Only very small variations can be detected, in contrast to the large deviations found in Yudhistira & Skote (2011) when shorter intervals were chosen. Hence, the turbulence statistics can be considered stationary and will in the following be taken from the interval  $t = 5000$ – $22\,000$ , which corresponds to  $\Delta t^+ = 19\,400$  in wall units.

### 3. Analytical derivations

In this section the time-averaged Navier–Stokes equations will be used and we denote the velocity components  $u_i$  (or  $u, v, w$ ), while the fluctuating part is denoted with a prime so that  $\tilde{u}_i = u_i + u'_i$ . Furthermore, we will focus on the case with streamwise modulated wall velocity since the case of temporal oscillations has been analysed in Skote (2012).

Starting from the laminar (as an approximation for the turbulent flow) spanwise momentum equation, and assuming parallel flow, an analytical expression for the spanwise shear can be found (§ 3.1), and by neglecting the transient regions at the beginning and end of the streamwise oscillation of wall velocity, the spanwise velocity profile can be derived (§ 3.2). The analytical expressions are compared with the (turbulent) DNS data.

#### 3.1. Spanwise shear

Here, the analysis will follow Viotti *et al.* (2009) until (3.7). Thereafter, additional issues need to be considered due to the spatially developing boundary layer.

By taking into account spanwise invariance and stationary flow, the spanwise momentum equation can be written as

$$u \frac{\partial w}{\partial x} + v \frac{\partial w}{\partial y} = \nu \left( \frac{\partial^2 w}{\partial x^2} + \frac{\partial^2 w}{\partial y^2} \right). \quad (3.1)$$

The Reynolds stress gradient terms in the spanwise momentum equation,

$$\frac{\partial \overline{u'w'}}{\partial x} \quad \text{and} \quad \frac{\partial \overline{v'w'}}{\partial y}, \quad (3.2)$$

are several magnitudes lower than the rest of the terms, as shown by Ricco & Quadrio (2008).

In the approximation of parallel flow ( $v = 0$ ) and by assuming that the spatial Stokes layer (SSL) is thin, the second-to-last term in (3.1) can be neglected, and (3.1) can be simplified to (Viotti *et al.* 2009):

$$u \frac{\partial w}{\partial x} = \nu \frac{\partial^2 w}{\partial y^2}. \quad (3.3)$$

Furthermore, the streamwise velocity  $u$  can be removed by replacing  $u(y)$  in (3.3) with the approximation

$$u \approx y \left. \frac{\partial u}{\partial y} \right|_{y=0}, \quad (3.4)$$

which is an accurate representation in this case since  $u^+ = y^+$  near the wall.

For the channel flow case, Viotti *et al.* (2009) derived the solution to (3.3) using the boundary condition

$$w(x, 0) = W_m \cos(\kappa x), \quad (3.5)$$

and the solution may be written as

$$w(x, y) = \frac{W_m}{\text{Ai}(0)} \text{Re} \left[ \exp(i\kappa x) \text{Ai} \left( -\frac{iy}{\delta_x} e^{-i4/3\pi} \right) \right], \quad (3.6)$$

where Ai is the Airy function and  $\kappa = 2\pi/\lambda_x$  is the forcing wavenumber. The thickness of the SSL is described by

$$\delta_x = \left( \frac{\nu^2 \lambda_x}{u_\tau^2 2\pi} \right)^{1/3}. \quad (3.7)$$

Expressed in wall units, (3.7) can be written as  $\delta_x^+ = (\lambda_x^+ / 2\pi)^{1/3}$ . We also note in (3.6) that the  $x$ -coordinate is scaled with  $\kappa$ , and the  $y$ -coordinate is scaled with  $\delta_x$  and hence we can form the non-dimensional vertical coordinate  $\eta = y/\delta_x$ . By introducing  $\kappa^+ = \kappa \nu / u_\tau$ , we can write  $\delta_x^+ = (\kappa^+)^{-1/3}$ , and hence  $\eta = y^+ (\kappa^+)^{1/3}$ .

Because we intend to retain the approximation of parallel flow for the present case, we introduce an averaged friction velocity, denoted by  $\bar{u}_\tau$ , which is defined as

$$\bar{u}_\tau = \frac{1}{L} \int_{x_i}^{x_f} (u_\tau) dx, \quad (3.8)$$

where  $L = x_f - x_i$ . The positions  $x_i$  and  $x_f$  are chosen so that  $u_\tau$  is relatively constant in the region over which the integration is taken. They are also specified such that a

full number of periods are covered. Hence, the positions numbered 0 and 8 in figure 2 are chosen, which in simulation coordinates correspond to  $x_i = 395.4$  and  $x_f = 453.0$ , respectively.

Thus, (3.3) can be formulated as

$$\bar{y} \frac{\partial \bar{w}}{\partial \bar{x}} = \frac{\partial^2 \bar{w}}{\partial \bar{y}^2}, \quad (3.9)$$

where the overbar ( $\bar{\quad}$ ) denotes wall-scaling based on the constant (averaged) friction velocity  $\bar{u}_\tau$ .

The boundary condition (BC) in this case is not a simple harmonic function. The spanwise wall velocity is shown in figure 2 (as the dotted line) and described by (2.6). However, as a analytical solution is sought, the BC must be expressed in cosine functions. Noting that a sinusoidal variation with amplitude of unity in the positive half-plane (of the  $x$ -axis) and zero value in the negative can be expressed as

$$\frac{1}{2} \cos\left(\kappa x + \frac{3\pi}{2}\right) + \frac{1}{2} \cos\left(|\kappa x| + \frac{3\pi}{2}\right), \quad (3.10)$$

the full BC given by (2.6) may be written:

$$w(x, 0) = \frac{W_m}{2} \left[ \cos\left(|\kappa(x - x_{start})| + \frac{3\pi}{2}\right) - \cos\left(|\kappa(x - x_{end})| + \frac{3\pi}{2}\right) \right], \quad (3.11)$$

with  $x_{start}$  and  $x_{end}$  specified as 250.3 and 483.0, respectively.

With this BC, the solution for the gradient of spanwise velocity at the wall becomes

$$\begin{aligned} \left. \frac{\partial w}{\partial y} \right|_{y=0} &= \frac{W_m}{2} \frac{Ai'(0)}{Ai(0)} \delta_x^{-1} \\ &\times \left[ \operatorname{sgn}(x_s) \sin\left(\kappa|x_s| + \frac{\pi}{2} - \frac{\pi}{3} \operatorname{sgn}(x_s)\right) - \operatorname{sgn}(x_e) \sin\left(\kappa|x_e| + \frac{\pi}{2} - \frac{\pi}{3} \operatorname{sgn}(x_e)\right) \right], \end{aligned} \quad (3.12)$$

where we have introduced the  $x$ -coordinates  $x_s \equiv x - x_{start}$  and  $x_e \equiv x - x_{end}$ . The function  $\operatorname{sgn}$  is the signum function. Note that (3.12) is the solution to (3.9) but is formulated in the unscaled variables. Hence,  $\delta_x$  has been evaluated using  $\bar{u}_\tau$  and is thus a constant in (3.12).

The analytical solution (3.12) is compared with DNS data for largest wall velocity (case 2) in figure 4, where the solid line is DNS data and the dotted line represent (3.12). The agreement is perfect except at the start of oscillation where the local  $u_\tau$  is very different from  $\bar{u}_\tau$  (the DR is still developing in this region: see figure 7), and at the end, where the sharp analytical solution is replaced by a gradual change due to the second-to-last term in (3.1) (which is neglected in the derivation of the analytical expression).

In the case of laminar boundary layers, the  $x$ -dependence of  $\delta_x$  can be derived, as was done by Ricco (2011), who found that  $\delta_x \sim x^{1/6}$ . This estimation can be provided because  $u_\tau \sim x^{-1/4}$  in the laminar case and hence the relation above follows directly from (3.7). On the other hand, in the present case,  $u_\tau$  can only be found as part of the solution of the streamwise momentum equation (this is the reason for introducing  $\bar{u}_\tau$  in the analysis above leading to the analytically solvable (3.9)), and will of course depend

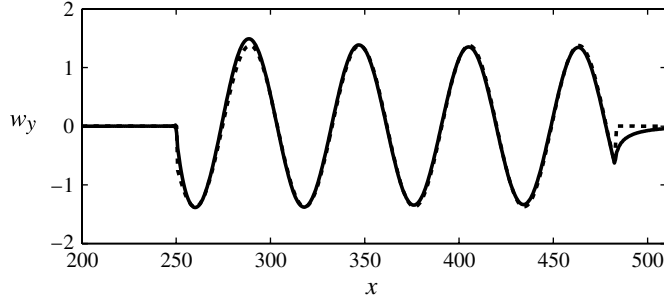


FIGURE 4. Downstream development of the spanwise velocity gradient from case 2: —, DNS data; ···, (3.12).

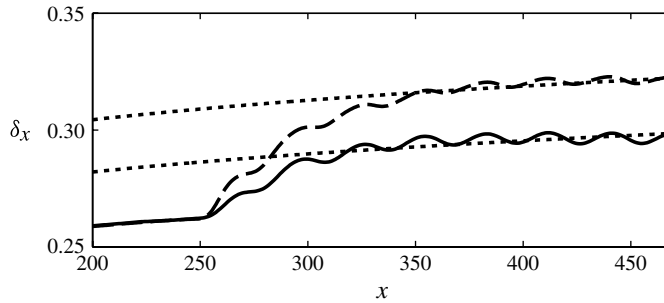


FIGURE 5. Downstream development of  $\delta_x$  compared with the estimation  $\delta_x \sim x^{1/15}$  indicated by the dotted lines; —, case 1; - -, case 2.

on the resulting DR. However, a rough estimation can be found if it is assumed that  $u_\tau$  varies (in  $x$ ) in approximately a similar way as for the unperturbed boundary layer, hence  $u_\tau \sim x^{-1/10}$  (see e.g. Schlichting 1979). Then it follows from (3.7) that  $\delta_x \sim x^{1/15}$ . This estimation is illustrated in figure 5 together with the  $\delta_x$  from cases 1 and 2. Even though  $\delta_x$  is oscillating in the downstream direction (which is a consequence of the streamwise variation of the DR), the general trend follows the rough estimate provided.

Note, however, that no enhancement of the accuracy of (3.12) is obtained by incorporating  $\delta_x \sim x^{1/15}$  as a replacement for a constant  $\delta_x$  based on  $\bar{u}_\tau$ , since (3.12) is a solution to (3.9) which was derived under the assumption of a constant  $u_\tau = \bar{u}_\tau$ .

### 3.2. Spanwise velocity profile

When deriving the analytical expression for the full spanwise velocity profile, we focus on the region over the oscillating part of the plate and do not consider either the spatially developing flow near the start of oscillation or the region close to the end of the oscillation. In this region, the spanwise velocity profile is derived from (3.9) with the BC:

$$w(x, 0) = W_m \cos\left(\kappa x_s + \frac{3\pi}{2}\right). \quad (3.13)$$

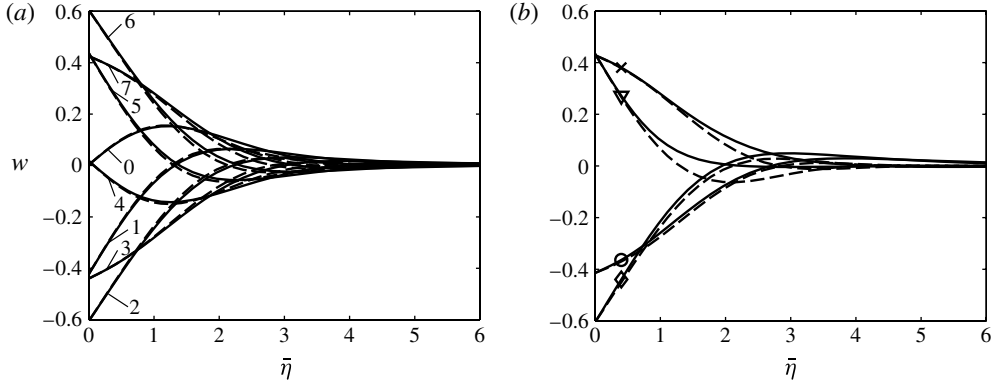


FIGURE 6. Spanwise velocity profiles for case 2: (a) at points labelled 0–7 in figure 2, (b) at points directly downstream from the start of oscillation. Lines: —, DNS; – –, from (3.14). Symbols:  $\nabla$ ,  $1/8\lambda_x$ ;  $\times$ ,  $3/8\lambda_x$ ;  $\diamond$ ,  $6/8\lambda_x$ ;  $\circ$ ,  $7/8\lambda_x$ .

The solution can be written as

$$w(x, y) = \frac{W_m}{\text{Ai}(0)} \text{Re} \left[ \exp \left( ikx_s + \frac{3\pi}{2} \right) \text{Ai}(-i\bar{\eta}e^{-i4/3\pi}) \right], \quad (3.14)$$

where  $\bar{\eta} = y\kappa^{1/3}(\bar{u}_\tau/\nu)^{2/3}$ .

The profiles from (3.14) are compared with the DNS data at eight points labelled as 0–7 in figure 2: thus, where the wall velocity is at its maximum and minimum levels, zero (points 0 and 4), and four positions in between. As the results in figure 6(a) indicate, the overlap is very good. Thus, even in the boundary layer flow, where the flow is inhomogeneous in the downstream direction (and hence  $u_\tau$  is not constant in contrast to channel flow), the spanwise velocity profile follows the prediction derived from the laminar equations. Good agreement was also found by Viotti *et al.* (2009) for channel flow where the theoretical profile is given by (3.6). For the temporal oscillation cases, similarly good agreement between DNS data and the classical Stokes solution was found (Skote 2012).

To investigate how soon downstream (3.14) is valid, the spanwise velocity profile immediately after the onset of wall oscillation is shown in figure 6(b). The agreement is not good until the end of the first wavelength of the forcing has been reached. Thus, the spatial transient for the spanwise flow is around one wavelength of the forcing. Remember that (3.14) is derived assuming constant  $u_\tau = \bar{u}_\tau$ , a condition which is clearly not fulfilled close to the onset of the forcing. Note that this relatively short spatial transient (one wavelength) only exists for the spanwise flow evolution. For the streamwise flow, the region of spatial development is longer, e.g. the transients of  $\delta_x$  (figure 5) are around 100 in  $x$ , corresponding approximately to two wavelengths of the forcing. Similar differences in the spanwise and streamwise flow development, respectively, were also found to exist in the time-dependent forcing of channel flow (Quadrio & Ricco 2003) and boundary layer flow (Skote 2012).

#### 4. Drag reduction and power budget

This section starts with a presentation of the DR (4.1), which is followed by an investigation of the energy saving budget (4.2).

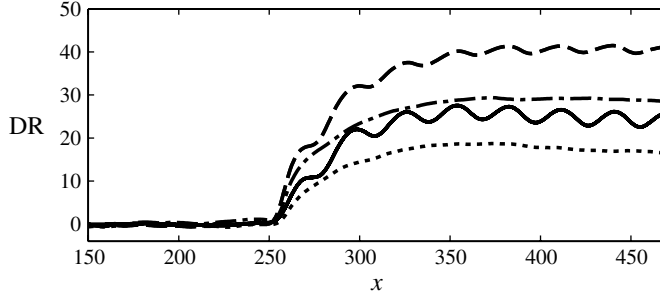


FIGURE 7. Downstream development of the DR. Present case 1 (—) and case 2 (---); temporal simulation results from Skote (2012) temp 1 (···) and temp 2 (- · -).

#### 4.1. Drag reduction

The friction coefficient is defined as

$$C_f = 2 \left( \frac{u_\tau}{U_\infty} \right)^2, \quad (4.1)$$

where the friction velocity  $u_\tau$  is calculated from the mean streamwise velocity gradient at the wall:

$$u_\tau \equiv \sqrt{\nu \left. \frac{\partial u}{\partial y} \right|_{y=0}}. \quad (4.2)$$

The resulting DR is calculated by

$$\text{DR}(\%) = 100 \frac{C_f^0 - C_f}{C_f^0}, \quad (4.3)$$

where  $C_f^0$  is the skin friction of the reference case. The downstream development of the DR is shown in figure 7, where case 1 is represented by the solid line and case 2 by the dashed line. Also included in the figure are the DR from temp 1 and 2, illustrated by the dotted and dash-dotted lines respectively. As noted in the figure, the DR for the spatial forcing is substantially larger than the corresponding temporal oscillation cases. The (spatial) oscillations in the DR clearly seen in figure 7 are a direct result of the downstream modulation of the wall velocity, and were investigated by Skote (2011).

The results in figure 7 are summarized in table 1, where the DR is calculated as a mean value over the portion of the flow where DR is constant (apart from the harmonic oscillations). In the cases presented here, the portion is chosen to be identical to the previous section, i.e. the region between  $x = 395.4$  and  $x = 453.0$ . For completeness we also include data from the two previous simulations performed by Skote (2011) and Yudhistira & Skote (2011), even though the wavelength and period, respectively, are slightly different in those cases ( $\lambda_x^+ = 1300$  and  $T^+ = 118$ , respectively).

#### 4.2. Energy saving

The energy saving due to DR is compared to the energy required to move the wall by estimating the idealized power consumption, following the derivation by Quadrio

Spatial oscillation			Temporal oscillation		
$W_m^+$	$\lambda_x^+$	DR	$W_m^+$	$T^+$	DR
6	1320	25.1	6 <sup>a</sup>	132	18.0
12	1320	41.0	12 <sup>a</sup>	132	29.4
17 <sup>b</sup>	1300	46.0	17 <sup>c</sup>	118	36.5

TABLE 1. Comparison of DR between spatial and temporal oscillations. <sup>a</sup> Data taken from Skote (2012). <sup>b</sup> Data taken from Skote (2011). <sup>c</sup> Data taken from Yudhistira & Skote (2011).

*et al.* (2009) and extended to boundary layer flow. The percentage saved power  $P_{sav}$  is equal to the percentage of friction DR (equation (4.3)), and integrated over a distance with approximately constant DR and integer number of periods (in this case  $x = 395.4\text{--}453.0$ ). The required percentage power  $P_{req}$  is similarly defined in terms of the friction power of the reference flow and may be written as

$$P_{req}(\%) = 100 \int_{x_i}^{x_f} v \frac{\partial w}{\partial y} \Big|_{y=0} W \, dx \Big/ \int_{x_i}^{x_f} (u_\tau^0)^2 U \, dx. \tag{4.4}$$

In addition, an integration in the spanwise direction ( $z$ ) is required, but is omitted in the formula above since the flow is homogeneous in that direction. In addition, a factor equal to density (of the fluid) times area (of the oscillating part of the bottom wall) is removed (cancelled out) in both numerator and denominator.

The net percentage power saving is defined as  $P_{net} = P_{sav} + P_{req}$  and is calculated to be 16.3 and 7.2% for the two cases presented here. The results presented by Viotti *et al.* (2009) showed that  $P_{net}$  becomes positive (up to 23%) for lower amplitudes of the forcing ( $W_m^+ = 6$ ). The larger value of  $P_{net}$  in their case is probably due to the lower  $Re$ ; see the discussion of Reynolds number dependence in Skote (2012).

Thus, the power saving for the two present cases is positive, in contrast to the high amplitude ( $W_m^+ = 17$ ) simulation by Skote (2011) which yielded  $P_{net} = -19.5$ . If  $P_{net}$  is negative it means that the power needed to drive the wall in the spanwise direction is greater than the power saved by streamwise DR.

For the temporally oscillating case, the percentage power  $P_{req}(\%)$  required to oscillate the wall may be written as (Skote 2012)

$$P_{req}(\%) = 100 \frac{W_m^2}{2} \sqrt{\nu\omega/2} \Big/ \frac{U}{L} \int_{x_i}^{x_f} (u_\tau^0)^2 \, dx, \tag{4.5}$$

where  $L = x_f - x_i$  and the integration is over a distance with approximately constant DR (in this case  $x = 366\text{--}468$ ).

The required power for all four cases is compared with the energy saving in table 2, together with the earlier simulations by Skote (2011) and Yudhistira & Skote (2011). Observe that the  $P_{net}$  is much lower for the temporal cases, in agreement with the channel flow simulations by Viotti *et al.* (2009).

### 5. Turbulence statistics

Due to the streamwise modulated wall forcing (for cases 1 and 2), the flow field is expected to be varying in the downstream direction. However, the streamwise velocity profile (as shown in figure 3a) is almost invariant when comparing different streamwise locations. A two-dimensional contour plot is shown in figure 8(a), where

$W_m^+$	Spatial oscillation			Temporal oscillation			
	$P_{sav}$	$P_{req}$	$P_{net}$	$W_m^+$	$P_{sav}$	$P_{req}$	$P_{net}$
6	25.1	-8.8	16.3	6 <sup>a</sup>	18.0	-15.2	2.85
12	41.0	-33.8	7.2	12 <sup>a</sup>	29.4	-60.8	-31.5
17 <sup>b</sup>	46.0	-65.5	-19.5	17 <sup>c</sup>	36.5	-133	-96.5

TABLE 2. Comparison of percentage power saving and required power for the spatial and temporal oscillations. The two first lines are the present data with  $\lambda_x^+ = 1320$  and  $T^+ = 132$  respectively, while slightly different values were used in the additional cases presented in the last row. <sup>a</sup>Data taken from Skote (2012). <sup>b</sup>Data taken from Skote (2011) ( $\lambda_x^+ = 1300$ ). <sup>c</sup>Data taken from Yudhistira & Skote (2011) ( $T^+ = 118$ ).

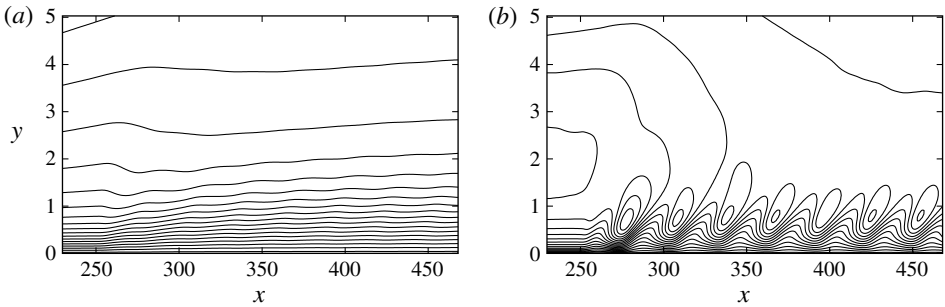


FIGURE 8. Two-dimensional plot stretched in the wall-normal direction. Streamwise dimension  $x = 230\text{--}468$ ; wall-normal  $y = 0\text{--}5$ . (a) Time-averaged and spanwise averaged streamwise velocity. Contour range from 0.025 to 0.0875 with spacing of 0.05. (b) Time-averaged and spanwise averaged spanwise Reynolds stress (r.m.s. value),  $(\overline{w'w'})^{1/2}$ . Contour range from 0.0025 to 0.0725 with spacing of 0.005.

only a very weak streamwise oscillation can be detected. On the other hand, the spanwise Reynolds stress, visualized for the same region in figure 8(b), exhibits a wildly fluctuating pattern in the downstream direction. (All Reynolds stresses exhibit harmonic oscillations downstream, but the spanwise component is by far the most distinctly varying.) For this reason, the turbulence statistics is presented in two sections below. First, the streamwise averaged profiles will be presented in § 5.1, where the averaging is taken over one period in the downstream direction. The result will be compared with the temporally oscillating case from which the profiles are averaged over a region of constant DR. Thereafter, in § 5.2, the spanwise Reynolds stress is investigated for various streamwise positions, and compared with the equivalent positions in time (phases) from the temporally oscillating case.

### 5.1. Averaged profiles

The longitudinal (r.m.s. value), normal (r.m.s. value), and shear Reynolds stresses respectively (averaged from  $x = 395.4$  to  $x = 453.0$ ) scaled with  $u_\tau^0$  are shown in figure 9(a). Profiles from case 2 are shown, together with the reference profiles (the thicker curves). For case 1 the profiles are located between the reference and case 2 curves (omitted in the figure for clarity).

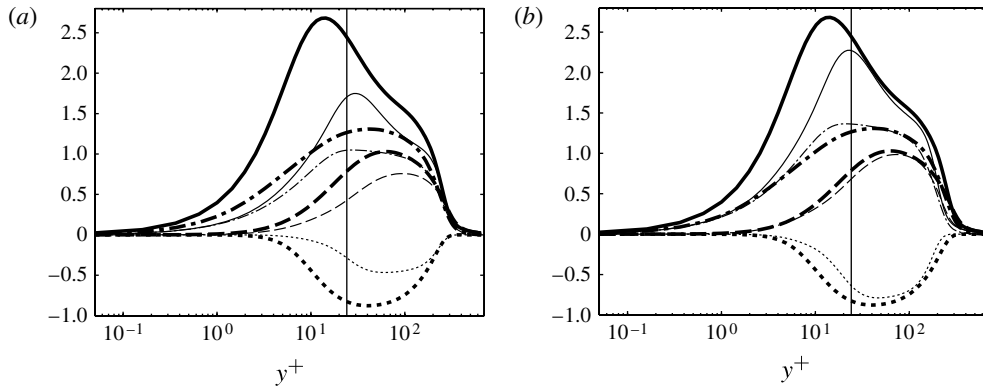


FIGURE 9. Reynolds stresses: —,  $u_{rms}^+$ ; --,  $v_{rms}^+$ ; - · -,  $w_{rms}^+$ ; ···,  $\overline{u'v'}$ . The thicker curves are the unmanipulated boundary layer; the thinner curves are for the spatially oscillating wall (case 2). (a) Reynolds stresses from the oscillating boundary layer scaled with  $u_\tau^0$ . (b) Reynolds stresses from the oscillating boundary layer scaled with  $\bar{u}_\tau$ .

The reductions in maximum  $u_{rms}^+$ , for cases 1 and 2, are 21 and 35% respectively, and 17% for case 1 and 26% for case 2 in maximum  $v_{rms}^+$ . For  $w_{rms}^+$ , the peak value is reduced by 11 and 20%, respectively. For the Reynolds shear stress  $\overline{u'v'}$  the reductions are larger; 28 and 47% for cases 1 and 2, respectively. The effect of the spatial wall forcing on the Reynolds stresses follows that observed from the temporal oscillations, although the reductions are augmented.

A line is added in figure 9(a) which corresponds to  $y^+ = 24.2$ , which marks the edge of the spatial Stokes layer (SSL), which is calculated from the velocity profile (figure 6).

When comparing the position of the maxima of the Reynolds stresses for the reference case, one may note that the peak of the longitudinal Reynolds stress ( $u_{rms}$ ) is located below the edge, while the normal, spanwise and shear stress peaks are positioned above. Thus, it might be suspected that the maximum in  $u_{rms}$  is affected more by the spatial Stokes layer than the other stresses. In order to investigate this, the stresses in figure 9(a) are scaled with the actual friction velocity  $\bar{u}_\tau$  and plotted in figure 9(b). In agreement with the reasoning above, the peak in  $u_{rms}$  is greatly affected while normal and shear stress peaks exhibit much less reduction. Similar features were found in the temporal case by Skote (2012). Note that there also exists a strong similarity in the Reynolds stresses between the present boundary layer flow and channel flow with temporal forcing; see e.g. the simulation results by Ricco *et al.* (2012).

In figure 9 it is also noteworthy that the peak values of  $u_{rms}$ ,  $v_{rms}$  and  $\overline{u'v'}$  have shifted further away from the wall in the wall forcing case, while on the other hand the peak of  $w_{rms}$  has moved closer to the wall.

Comparison of the longitudinal Reynolds stress for all four cases (we compare case 1 with temp 1, and case 2 with temp 2) in figure 10(a) reveals that the reduction (compared with the reference case) is similar for both types of wall oscillations even though the DR is much higher for the spatial cases. Again, all the profiles in figure 10 have been averaged over  $x = 395.4\text{--}453.0$  in the spatial cases, while the region  $x = 366.0\text{--}468.0$  is used for averaging in the temporal cases. For  $v_{rms}$  and  $\overline{u'v'}$  (not shown in figure 10a), the profiles from all four cases are very similar. The Reynolds

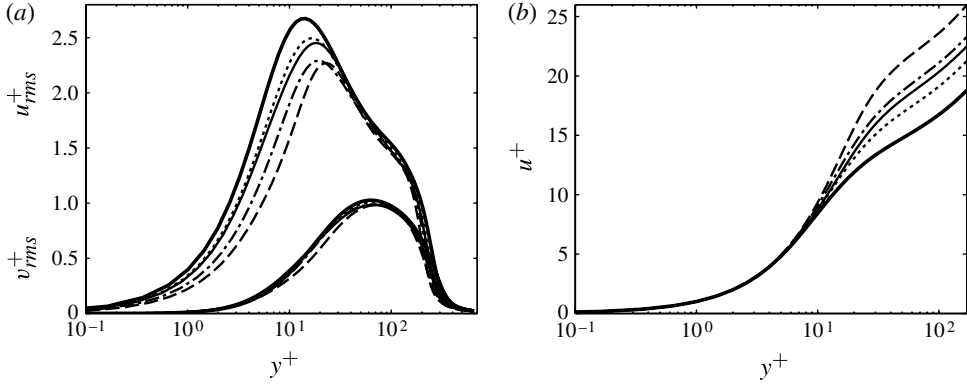


FIGURE 10. (a) Longitudinal and normal Reynolds stresses scaled with  $\bar{u}_\tau$ . (b) Velocity profile scaled with  $\bar{u}_\tau$ . Thick solid line, reference case; thin solid line, case 1; — —, case 2;  $\cdots$ , temp 1; — · —, temp 2.

stress component that exhibits the most differences between spatial and temporal cases (and thus accounts for the different DR) is  $w_{rms}$ , which will be investigated in § 5.2 below.

In contrast to the Reynolds stresses, the velocity profiles exhibit more pronounced differences, as seen in figure 10(b). The figure demonstrates that the DR is directly related to the velocity profiles by the upward shifting of the logarithmic layer. Only the inner part is shown in figure 10(b) for clarity; please refer to figure 3(b) for the full profile. By comparing the velocity profiles from all four cases we note that the viscous linear region is present in all cases while the shifting of the logarithmic region is clearly correlated to the amount of DR. Thus, the response of the velocity profile to the wall forcing is fundamentally different from the shear stress decreasing effect from an adverse pressure gradient, which alters the scaling in the near-wall region by a change of velocity scale: see Skote & Henningson (2002).

### 5.2. Spatially varying spanwise Reynolds stress

Although the streamwise modulated spanwise wall forcing results in a very weakly oscillating streamwise velocity (see figure 8a), the spanwise Reynolds stress is strongly varying (figure 8b). Hence, the streamwise averaged (over one wavelength) profiles of the Reynolds stresses shown in figure 9 cannot provide the full detailed picture.

The  $w_{rms}$  profiles at positions 1–8 (referring to figure 2) are investigated next in order to elucidate the spatial variation. First, however, the  $w_{rms}$  for case 2 and temp 2 are compared in figure 11(a). The solid line is the  $w_{rms}$  from temp 2, which will eventually reach a value of  $W_m/\sqrt{2}$  at the wall due to the temporal wall forcing. In order to remove this effect from the temporal Stokes layer, a phase averaging over one period is done, as indicated by the dash-dotted line. As can be seen in figure 11(a), above the Stokes layer, the two profiles coincide. The profile from the spatial forcing (the dotted line) is located below the temporal one, and hence this is the most significant difference between the two types of forcing. Remember that the longitudinal and wall-normal stresses were almost identical for the temporal and spatial cases (for the same set of oscillation parameters) even though the DR is significantly different.

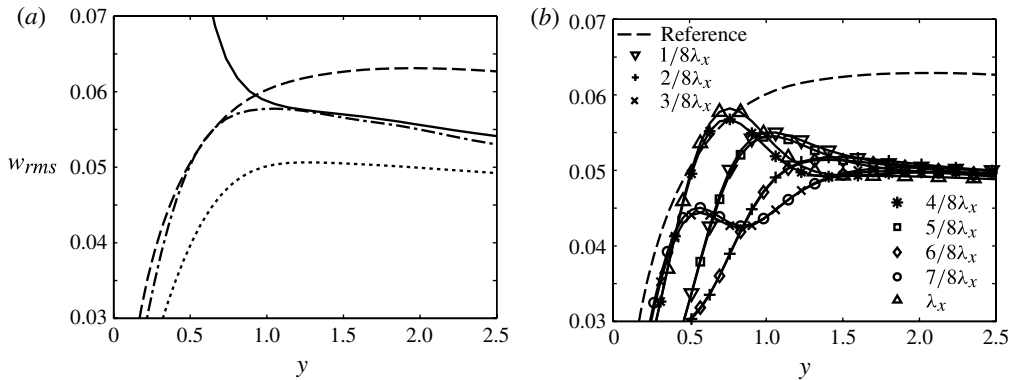


FIGURE 11. (a) Spanwise Reynolds stress ( $w_{rms}$ ): —, reference case;  $\cdots$ , case 2; —, temp 2; — · —, temp 2, phase-averaged over one period. (b) Fully developed  $w_{rms}$  profiles for case 2 at spatial positions indicated in the legend, which correspond to positions 1–8 in figure 2.

The simulation scaling has been retained in figures 11 and 12 (i.e. free stream velocity  $U$  for  $w_{rms}$  and inlet displacement thickness  $\delta^*$  for the vertical coordinate  $y$ ). The reference case is indicated by the dashed line in all the figures.

The comparison between different downstream positions is made in figure 11(b) in the region after the spatial transients. Clearly the  $w_{rms}$  is periodic with wavelength  $\lambda_x/2$ . Thus, the detailed study of each position over one wavelength reveals a complex pattern.

When comparing with some of the profiles at the corresponding spatial phase in the region where the flow is still developing (figure 12a), it is noted that the profile at  $3/8\lambda_x$  has not yet developed its characteristic double peak feature that was observed in the developed region. In addition, the peak is much larger here than further downstream. On the other hand, the profile at  $7/8\lambda_x$  does exhibit the double peak feature and hence the flow is already maturing at this point, although the value is larger than further downstream. To confirm this, the profile at the end of the first full cycle (at  $\lambda_x$ ) is plotted, and indeed it has the same shape as the profile at the corresponding phase further downstream, but the value is still larger (around 20%). The three profiles in figure 12(a) are taken from positions 9–11 (referring to figure 2).

To be possible to compare with the temporal simulation, the profiles in this case must be taken from corresponding phases in time. The profiles for some representative phases are shown in figure 12(b) with the same symbols as in the two previous illustrations. At  $t = 1/8T$  and  $t = 5/8T$  the peaks are stronger than in the spatial simulation, which explains to a certain degree why the DR is weaker in this case. At the phases  $t = 4/8T$  and  $t = T$  (corresponding to  $4/8\lambda_x$  and  $\lambda_x$  in the spatial case), there is a small indication of a double peak feature which was observed as much stronger in a different phase ( $3/8\lambda_x$  and  $7/8\lambda_x$ ) in the spatial case. On the other hand, the corresponding profiles in the temporal case at  $t = 3/8T$  and  $t = 7/8T$  do not exhibit the double peak.

### 5.3. Spanwise Reynolds stress production

When seeking an explanation for the reduction in spanwise Reynolds stress for the spatial case, it is natural to look at the production term in the transport equation for

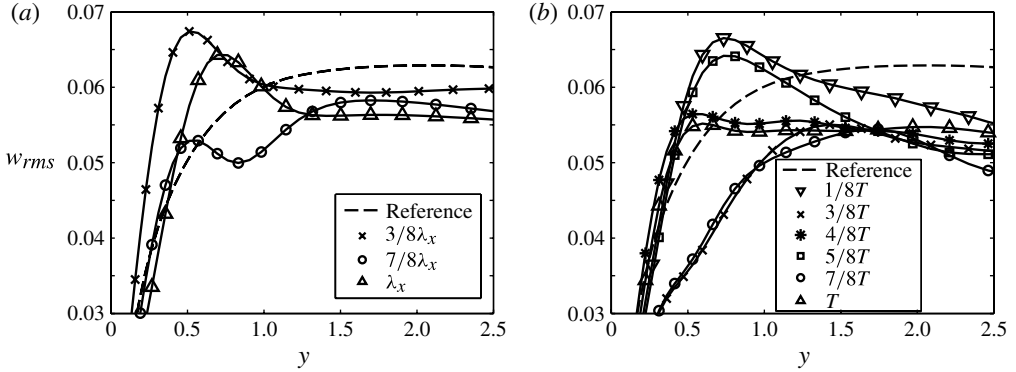


FIGURE 12. (a) Spatially developing  $w_{rms}$  profiles for case 2 at spatial positions indicated in the legend, which correspond to positions 9–11 in figure 2. (b) Fully developed  $w_{rms}$  profiles for temp 2 at time instances indicated in the legend.

this component:

$$\mathcal{P}_{33} = \mathcal{P}_{vw} + \mathcal{P}_{uw} = -2\overline{v'w'}\frac{\partial w}{\partial y} - 2\overline{u'w'}\frac{\partial w}{\partial x}. \quad (5.1)$$

Both  $\mathcal{P}_{vw}$  and  $\mathcal{P}_{uw}$  are zero for the unforced boundary layer, while the latter is zero in the temporal forcing case. In contrast, both terms are non-zero for the spatial forcing case. The two production terms in (5.1) are directly related to the wall oscillation since  $\partial w/\partial y$  and  $\partial w/\partial x$  are involved in  $\mathcal{P}_{vw}$  and  $\mathcal{P}_{uw}$ , respectively. The streamwise derivative ( $\partial w/\partial x$ ) is non-zero only for the spatially oscillating forcing. The two parts are shown in figure 13 for case 2, and reveal that  $\mathcal{P}_{uw}$  actually has a negative contribution to the production. Thus, the streamwise modulation of the forcing, which corresponds to  $\partial w/\partial x$ , creates a lower total production of  $\overline{w'w'}$ .

In order to compare with the temporal case the production term  $\mathcal{P}_{33}$  needs to be evaluated, which is a non-trivial task, as shown by earlier attempts. In the statistics from temporal forcing of the channel flow presented by Quadrio & Ricco (2003),  $\mathcal{P}_{33}$  was zero – excluding the initial transients, which were shown to be non-zero by both Quadrio & Ricco (2003) and Xu & Huang (2005). However, as demonstrated by Toubert & Leschziner (2012), the decomposition of the flow needs to be refined in the case of temporal forcing, and can be written as  $\tilde{u}_i = \langle u_i \rangle + u_i''$ , where  $\langle u_i \rangle$  is the phase-averaged  $\tilde{u}_i$ , and  $u_i''$  represents stochastic fluctuations, separated from the phase fluctuations;  $u_i''$  is related to the total fluctuation  $u_i'$  via  $u_i'' = u_i' - (\langle u_i \rangle - u_i)$ . Hence,  $u_i''$  is the total fluctuation with periodic fluctuations removed. With this formulation, as shown by Toubert & Leschziner (2012), the production becomes

$$\mathcal{P}_{33} = -2\overline{\langle v''w'' \rangle} \frac{\partial \langle w \rangle}{\partial y}. \quad (5.2)$$

An analogy can be made with the spatial case as follows. Consider the spatially averaged statistics over an integer number of wavelengths (of the forcing). Then, both  $\overline{v'w'}$  and  $\partial w/\partial y$  are zero, thus yielding a zero  $\mathcal{P}_{vw}$ . On the other hand, the spatially averaged  $\mathcal{P}_{vw} = \overline{v'w'}\partial w/\partial y$  (with the product calculated at each  $x$ -location, followed by an averaging in  $x$ ) yields the dotted curve in figure 13(a). Thus, the (spatial) phase

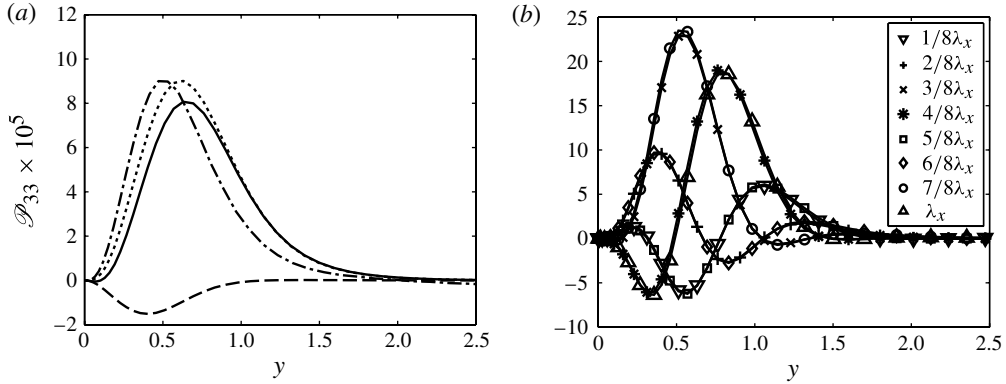


FIGURE 13. (a) The spanwise Reynolds stress production terms for case 2 and temp 2. Spatial forcing:  $\cdots$ ,  $\mathcal{P}_{vw}$ ;  $---$ ,  $\mathcal{P}_{uw}$ ;  $- \cdot -$ ,  $\mathcal{P}_{33} = \mathcal{P}_{vw} + \mathcal{P}_{uw}$ . Temporal forcing:  $- \cdot -$ ,  $\mathcal{P}_{33}$  according to (5.2). (b)  $\mathcal{P}_{33}$  profiles for case 2 at spatial positions indicated in the legend, which correspond to positions 1–8 in figure 2.

average is clearly different compared to the spatial average, hence in analogy with the temporal case.

The  $\mathcal{P}_{33}$  resulting from (5.2) is included in figure 13(a) as the dash-dotted line. Clearly, the production is of similar magnitude to the production from the first term in (5.1) and hence the negative contribution from the second term explains (at least partially) the lower values of  $w_{rms}$  and consequently the larger DR in the case with spatial forcing.

The individual  $\mathcal{P}_{33}$  for case 2 at different phases are shown in figure 13(b) and indicate that the behaviour through the various stages of one wavelength is rather complicated. In addition, by comparing to the  $w_{rms}$  in figure 11(b), it is noted that the positions with maximum production are not equal to the phase with maximum  $w_{rms}$ , and hence all terms in the  $w_{rms}$  budget need to be considered, as well as the complete budgets of all the other Reynolds stresses (due to the inter-component energy transfer), for the complete picture.

The analysis presented in this section provides no definite information as to why the shear stress at the wall decreases. However, it does shed some light on why the spanwise Reynolds stress is reduced more in the spatial case than in the temporal case, hence giving a clue as to why the spatial forcing is more efficient at reducing the viscous drag compared to the temporal forcing.

## 6. Conclusion

Direct numerical simulations have been performed to study the effect of spatial and temporal wall oscillations with two different wall velocities on the turbulent boundary layer. The resulting drag reduction is larger for the spatial oscillation, in agreement with findings from channel flow simulations.

An estimation of the idealized power consumption shows that the positive energy budget is greater for the weaker wall velocity case (in agreement with channel flow). In the case of very high wall velocity, more energy is required for the spatial oscillation than what is saved by DR, although the DR is enhanced compared to the weaker wall velocity cases.

The streamwise variation of the spanwise shear from the onset of spatial oscillations is in good agreement with the analytical solution to the laminar Navier–Stokes equations. In addition, comparisons of the spanwise velocity profiles at various phases with the analytical solution show very good agreement. Furthermore, the spatial transients are shown to be confined to the first wavelength of the wall forcing. The short transients only occur for the spanwise flow, while the streamwise flow (for example the DR) exhibits longer spatial transients.

The streamwise development of the spatial Stokes layer was theoretically found to vary as  $\sim x^{1/15}$ , and this estimation follows the trend observed in the DNS data.

The Reynolds stresses are reduced by the oscillations and the effect on the maximum depends on whether the position of the maximum is inside or outside the spatial Stokes layer formed due to the streamwise modulated wall velocity.

Comparing the Reynolds stresses from the spatial and temporal wall forcing cases revealed that only the spanwise component is considerably lower for the spatial forcing case, and thus accounts for the larger DR in this case. The spatial variation of the spanwise Reynolds stress is periodic with a wavelength half of the wall forcing. Comparison with the profiles from the temporal wall forcing case showed that the latter are generally of a larger value even though the distinct double peak visible in the spatial case at phases  $3/8\lambda_x$  and  $7/8\lambda_x$  is lacking in the temporal profiles.

The lower spanwise Reynolds stress for the spatial forcing case is (at least partially) explained by the reduced production term. The attenuation is provided by a second term involving the streamwise gradient of the spanwise velocity. Comparison with the temporal case involved scrutinizing earlier statistics, and by utilizing new DNS data from our own temporal forcing, the non-zero production of spanwise Reynolds stress is confirmed. Furthermore, the production is of a similar magnitude to the spatial case.

This investigation (of the turbulence production) points to the difficulties involved when defining the correct terms and the interpretations thereof.

In future work, apart from a continued effort to understand the DR mechanisms from a fundamental point of view, a parametric map as provided by Viotti *et al.* (2009) or Quadrio *et al.* (2009) for channel flow (the latter for travelling wave forcing), giving the optimal parameters for DR would be welcome for the boundary layer flow. However, the number of simulations to be performed in order to provide such a map is prohibitively large and time-consuming. Perhaps a better approach would be to utilize nonlinear optimization techniques, such as demonstrated by Hasegawa & Kasagi (2011) for identifying the optimal set of parameters. Furthermore, as has been shown by Skote (2012), the dependence on the parameters is likely to be similar for the two types of flows, so that conclusions drawn from channel flow can be utilized for the boundary layer. On the other hand, as the Reynolds number dependence has not yet been addressed properly (Skote 2012), the validity and usefulness of such a parametric map is limited since it will probably depend strongly on the Reynolds number.

Another approach for future work could be on the applicability of the methods in real applications. An excellent example of this is presented by Ricco & Hahn (2013), who utilize rotating discs instead of letting the whole wall oscillate. Innovative ideas such as these could fast-forward the applicability of DR techniques, while the slower-paced fundamental research, of which the present article is an example, could provide deeper understanding and eventually lead to more efficient means of DR.

## Acknowledgements

Academic Research Fund Tier 1 (RG 37/10) from Ministry of Education, Singapore, is greatly acknowledged. Computer time from the High Performance Computing Centre at Nanyang Technological University was invaluable for the completion of the simulations.

## REFERENCES

- AUTERI, F., BARON, A., BELAN, M., CAMPANARDI, G. & QUADRIO, M. 2010 Experimental assessment of drag reduction by traveling waves in a turbulent pipe flow. *Phys. Fluids* **22**, 115103.
- BARON, A. & QUADRIO, M. 1996 Turbulent drag reduction by spanwise wall oscillations. *Appl. Sci. Res.* **55**, 311–326.
- CHEVALIER, M., SCHLATTER, P., LUNDBLADH, A. & HENNINGSON, D. S. 2007 SIMSON: a pseudo-spectral solver for incompressible boundary layer flows. *Tech. Rep.* TRITA-MEK 2007:07, KTH Mechanics, Stockholm, Sweden.
- CHOI, K.-S. 2002 Near-wall structure of turbulent boundary layer with spanwise-wall oscillation. *Phys. Fluids* **14**, 2530–2542.
- CHOI, K. S. & CLAYTON, B. R. 2001 The mechanism of turbulent drag reduction with wall oscillation. *Intl J. Heat Fluid Flow* **22** (1), 1–9.
- CHOI, K. S. & GRAHAM, M. 1998 Drag reduction of turbulent pipe flows by circular-wall oscillation. *Phys. Fluids* **10** (1), 7–9.
- CHOI, J.-I., XU, C. X. & SUNG, H. J. 2002 Drag reduction by spanwise wall oscillation in wall-bounded turbulent flows. *AIAA J.* **40** (5), 842–850.
- DI CICCIA, G. M., IUSO, G., SPAZZINI, P. G. & ONORATO, M. 2002 Particle image velocimetry investigation of a turbulent boundary layer manipulated by spanwise wall oscillations. *J. Fluid Mech.* **467**, 41–56.
- DUGGLEBY, A., BALL, K. S. & PAUL, M. R. 2007 The effect of spanwise wall oscillation on turbulent pipe flow structures resulting in drag reduction. *Phys. Fluids* **19**, 125107.
- HASEGAWA, Y. & KASAGI, N. 2011 Dissimilar control of momentum and heat transfer in a fully developed turbulent channel flow. *J. Fluid Mech.* **683**, 57–93.
- JUNG, W. J., MANGIACACCHI, N. & AKHAVAN, R. 1992 Suppression of turbulence in wall-bounded flows by high-frequency spanwise oscillations. *Phys. Fluids A* **4** (8), 1605–1607.
- KARNIADAKIS, G. E. & CHOI, K. S. 2003 Mechanisms on transverse motions in turbulent wall flows. *Annu. Rev. Fluid Mech.* **35**, 45–62.
- KASAGI, N., SUZUKI, Y. & FUKAGATA, K. 2009 Microelectromechanical systems-based feedback control of turbulence for skin friction reduction. *Annu. Rev. Fluid Mech.* **41**, 231–251.
- LAADHARI, F., SKANDAJI, L. & MOREL, R. 1994 Turbulence reduction in a boundary layer by a local spanwise oscillating surface. *Phys. Fluids* **6**, 3218–3220.
- NIKITIN, N. V. 2000 On the mechanism of turbulence suppression by spanwise surface oscillations. *Fluid Dyn.* **35** (2), 185–190.
- QUADRIO, M. & RICCO, P. 2003 Initial response of a turbulent channel flow to spanwise oscillation of the walls. *J. Turbul.* **4** (7), 1–23.
- QUADRIO, M. & RICCO, P. 2004 Critical assessment of turbulent drag reduction through spanwise wall oscillations. *J. Fluid Mech.* **521**, 251–271.
- QUADRIO, M. & RICCO, P. 2011 The laminar generalized Stokes layer and turbulent drag reduction. *J. Fluid Mech.* **667**, 135–157.
- QUADRIO, M., RICCO, P. & VIOTTI, C. 2009 Streamwise-travelling waves of spanwise wall velocity for turbulent drag reduction. *J. Fluid Mech.* **627**, 161–178.
- QUADRIO, M. & SIBILLA, S. 2000 Numerical simulation of turbulent flow in a pipe oscillating around its axis. *J. Fluid Mech.* **424**, 217–241.
- RICCO, P. 2004 Modification of near-wall turbulence due to spanwise wall oscillations. *J. Turbul.* **5** (24), 1–18.
- RICCO, P. 2011 Laminar streaks with spanwise wall forcing. *Phys. Fluids* **23**, 064103.

- RICCO, P. & HAHN, S. 2013 Turbulent drag reduction through rotating discs. *J. Fluid Mech.* **722**, 267–290.
- RICCO, P., OTTONELLI, C., HASEGAWA, Y. & QUADRIO, M. 2012 Changes in turbulent dissipation in a channel flow with oscillating walls. *J. Fluid Mech.* **700**, 77–104.
- RICCO, P. & QUADRIO, M. 2008 Wall-oscillation conditions for drag reduction in turbulent channel flow. *Intl J. Heat Fluid Flow* **29** (4), 601–612.
- RICCO, P. & WU, S. 2004 On the effects of lateral wall oscillations on a turbulent boundary layer. *Exp. Therm. Fluid Sci.* **29**, 41–52.
- SCHLATTER, P., ÖRLÜ, R., LI, Q., BRETHOUWER, G., FRANSSON, J. H. M., JOHANSSON, A. V., ALFREDSSON, P. H. & HENNINGSON, D. S. 2009 Turbulent boundary layers up to  $Re_\Theta = 2500$  studied through simulation and experiment. *Phys. Fluids* **21**, 051702.
- SCHLICHTING, H. 1979 *Boundary Layer Theory*, 7th edn. McGraw-Hill.
- SKANDAJI, L. 1997 Étude de la structure d'une couche limite turbulente soumise à des oscillations transversales de la paroi. PhD thesis, École Centrale de Lyon.
- SKOTE, M. 2011 Turbulent boundary layer flow subject to streamwise oscillation of spanwise wall-velocity. *Phys. Fluids* **23**, 081703.
- SKOTE, M. 2012 Temporal and spatial transients in turbulent boundary layer flow over an oscillating wall. *Intl J. Heat Fluid Flow* **38**, 1–12.
- SKOTE, M. & HENNINGSON, D. S. 2002 Direct numerical simulation of a separated turbulent boundary layer. *J. Fluid Mech.* **471**, 107–136.
- TOUBER, E. & LESCHZINER, M. A. 2012 Near-wall streak modification by spanwise oscillatory wall motion and drag-reduction mechanisms. *J. Fluid Mech.* **693**, 150–200.
- TRUJILLO, S. M., BOGARD, D. G. & BALL, K. S. 1997 Turbulent boundary layer drag reduction using an oscillating wall. *AIAA Paper* 97-1870.
- VIOTTI, C., QUADRIO, M. & LUCHINI, P. 2009 Streamwise oscillation of spanwise velocity at the wall of a channel for turbulent drag reduction. *Phys. Fluids* **21**, 115109.
- XU, C. X. & HUANG, W. X. 2005 Transient response of Reynolds stress transport to spanwise wall oscillation in a turbulent channel flow. *Phys. Fluids* **17**, 018101.
- YUDHISTIRA, I. & SKOTE, M. 2011 Direct numerical simulation of a turbulent boundary layer over an oscillating wall. *J. Turbul.* **12** (9), 1–17.